Accepted Manuscript

Please cite this article as: Nemanja D.Banić, Biljana F.Abramović, Jugoslav
B.Krstić, Daniela V.Šojić Merkulov, Nina L.Finčur, Miodrag N.Mitrić,
Novel WO3/Fe3O4 magnetic photocatalysts: Preparation, characterization
and thiacloprid photodegradation, Journal of Industrial and Engineering
Chemistry https://doi.org/10.1016/j.jiec.2018.10.025

Novel WO₃/Fe₃O₄ magnetic photocatalysts: Preparation, characterization and thiacloprid photodegradation

Nemanja D. Banić[1], Biljana F. Abramović[1]*, Jugoslav B. Krstić[2], Daniela V. Šojić Merkulov[1], Nina L. Finčur[1], Miodrag N. Mitrić[3]

[1]University of Novi Sad, Faculty of Sciences, Department of Chemistry, Biochemistry and Environmental Protection, Trg D. Obradovića 3, 21000 Novi Sad, Serbia
[2]Institute of Chemistry, Technology and Metallurgy, Department of Catalysis and Chemical Engineering, University of Belgrade, Njegoševa 12, 11000 Belgrade, Serbia
[3]Vinča Institute of Nuclear Sciences, University of Belgrade, Mike Petrovića Alasa 12-14, 11001 Belgrade, Serbia

*Professor Biljana Abramović
Department of Chemistry, Biochemistry and Environmental Protection
Faculty of Sciences
University of Novi Sad
Phone: +381 21 4852753
Fax: +381 21 454065
e-mail: biljana.abramovic@dh.uns.ac.rs
Trg D. Obradovića 3
21000 Novi Sad
Serbia

E-mail address: nemanja.banic@dh.uns.ac.rs (Nemanja D. Banić)
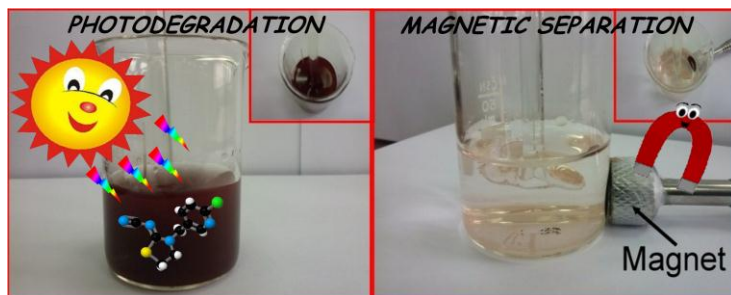   jkrstic@nanosys.ihtm.bg.ac.rs (Jugoslav B. Krstić)
                daniela.sojic@dh.uns.ac.rs (Daniela V. Šojić Merkulov)
                nina.fincur@dh.uns.ac.rs (Nina L. Finčur)
                mmitric@vinca.rs (Miodrag N. Mitrić)

Graphical abstract

Highlights:

- Four WO_3/Fe_3O_4 nanopowders were synthesized by chemical co-precipitation method.
- By increasing the content of WO_3, the magnetite phase content also increased.
- WO_3 can promote degradation efficiency of WO_3/Fe_3O_4 for thiacloprid removal.
- Content of WO_3 in synthesized catalysts affects the process of magnetic separation.

Abstract

This work presents the characterization of novel synthesized WO_3/Fe_3O_4 catalysts and investigates their photocatalytic activity for thiacloprid decomposition under UV and simulated sunlight radiation. Four WO_3/Fe_3O_4 nanopowders with different amounts of WO_3 were synthesized by chemical co-precipitation method. XRD analysis showed the presence of hematite and magnetite nano-dimensional phases of Fe_3O_4 in the catalysts. The magnetite phase content increased with increasing WO_3 content. Degradation efficiency of thiacloprid in the presence of $6.1WO_3/Fe_3O_4/H_2O_2$ under simulated solar radiation was 2.2 times higher compared to Fe_3O_4. Under an external magnetic field, a significant increase in the catalysts separation from reaction mixture was observed.

Keywords: WO_3/Fe_3O_4, Photodegradation, Thiacloprid, Hematite/magnetite, Magnetic separation.

1. Introduction

The enormous industrial development and growth of the human population has led to very serious environmental problems due to the uncontrolled release of harmful compounds [1,2]. The increasing use of pesticides, pharmaceuticals, lifestyle products, food additives, heavy metals and petroleum products has additionally contributed to the increase in

pollution [3]. Most of these compounds are characterized by high environmental stability. As a consequence, it has been reported that clean water supplies are struggling to meet ever-increasing demands. Water supply remains a significant global challenge, with the World Health Organization estimating that around 844 million people lack even basic drinking water services [4].

The so-called advanced oxidative processes (AOPs), oxidation processes which generally lead to the total mineralization of organic pollutants into harmless final products, have attracted a great deal of recent attention [5,6]. For the treatment of water pollution, a TiO_2 slurry is the most frequently applied method [7]. The main drawback of this method is that the suspended photocatalysts can be hard to separate from the treated water and are thus difficult to reuse. This issue is particularly relevant for nanomaterials, whose difficulty in separation hinders their practical application at industrial scales and leads to more pollution. One possible solution which is investigated herein, is the use of magnetic materials as a supporting material. Fe_3O_4 nanoparticles have the superparamagnetic property, which allows them to be easily separated from a suspension with an external magnetic field [8,9].

Many efforts have been made to develop light-driven photocatalysts in order to make good use of solar energy [10]. Although many different types of photocatalyst have been synthesized, most of them only show significant activity under the influence of UV irradiation, which accounts for only about 4% of the solar spectrum [11–15]. This imposes the necessity of applying the photo-Fenton process, which is the most suitable of all AOPs to utilise solar irradiation, because the soluble iron–hydroxyls and especially the iron–organic acid complexes, absorb not only UV irradiation but even part of the visible light spectrum. This system is very efficient for generating radicals for oxidative processes [16], especially at pH 2.8 [17], where approximately one half of the Fe(III) is present as the Fe^{3+} ion and the other half as $Fe(OH)^{2+}$ ion: a photo-active species. The main advantage of the photo-Fenton system is light sensitivity up to a wavelength of 600 nm [18].

Among the different organic substances that are known as water pollutants, pesticides are the main source of pollution for both ground and surface waters [19]. Neonicotinoids are a relatively new kind of insecticide, used in the past few decades to control various pests, especially whiteflies, sucking insect pests such as aphids, leafhoppers and planthoppers, some micro-Lepidoptera, thrips, and some coleopteran pests [20]. Studies of the environmental behaviour of neonicotinoid insecticide thiacloprid (TCL, (Z)-3-(6-chloro-3-pyridylmethyl)-1,3-thiazolidin-2-ylidenecyanamide) have shown that the molecule is resistant for more than six months to hydrolysis in acidic or neutral media, and that even

3

at pH 10, only 10% of TCL was degraded in aerated water over the same time scale [21,22]. Flash photolysis [23], photocatalytic ozonation [22,24], UV, UV/H_2O_2, $UV/Fe/TiO_2/H_2O_2$ [25,26], UV/ZnO, Vis/ZnO [27,28] and $Vis/Fe/TiO_2/H_2O_2$ [29] are all processes which have been used for TCL removal from water.

Although there are numerous examples of various synthesis methods for obtaining either Fe_3O_4 or WO_3 [30–34], synthesis of the WO_3/Fe_3O_4 photocatalyst is relatively rare. Besides, based on the available literature, precipitation of Fe species with WO_3 particles using subsequent calcination, used in this paper for synthesis of mentioned catalyst, was not studied yet. Especially, there is no case of WO_3/Fe_3O_4 using, synthesized in any way, for the photocatalytic degradation of TCL.

The objective of this study was to 1) prepare novel cost-effective WO_3/Fe_3O_4 materials with different WO_3 contents, 2) characterize them by a number of physicochemical methods (XRD, SEM, TEM, N_2 physisorption at -196 °C, SQUID and UV-Vis DRS), 3) test their photocatalytic activities using the example of TCL degradation under UV and simulated sunlight radiation in aqueous suspension containing H_2O_2, 4) use the best material obtained to study in detail TCL removal under a variety of experimental conditions, and 5) examine how the content of WO_3 in synthesized catalysts affects the efficiency of magnetic separation, which is of exceptional importance for separating and recovering catalyst particles.

2. Materials and methods

2.1. Materials

All chemicals were reagent grade and were used without further purification. Thiacloprid ($C_{10}H_9ClN_4S$, 99.9% purity) and 99.8% acetonitrile (ACN) were obtained from Sigma-Aldrich (USA); HCl and NaOH were purchased from ZorkaPharm (Šabac, Serbia); $Na_2WO_4 \cdot 2H_2O$ and H_2SO_4 were from Merck (Germany); $FeCl_3 \cdot 6H_2O$ and $FeSO_4 \cdot 7H_2O$ were obtained from Poch (Gliwice, Poland); 30% H_2O_2 was produced by Centrohem (Stara Pazova, Serbia); 85% H_3PO_4 was purchased from Lachema (Neratovice, Czech Republic) and $AgNO_3$ was obtained from Kemika (Zagreb, Croatia). All solutions were prepared using double distilled water.

2.2. Catalyst synthesis

WO_3 was first prepared using a method similar to that described by Gotić et al. [31]. Under vigorous magnetic stirring, 0.7 mol L^{-1} HCl was added to 50 mL of 1 mol L^{-1} Na_2WO_4 solution until the final pH of the clear solution reached a value of 1.4. The reaction solution was then warmed to 60 °C and held without stirring for 48 h. After this, the solid white product was separated from the mother liquor by filtration using a glass Buchner funnel. The white precipitate was then washed several times with double distilled water and dried at 60 °C for 48 h. The resulting WO_3 powder was placed in a desiccator and used for the further synthesis of WO_3/Fe_3O_4 composites. Four WO_3/Fe_3O_4 nanopowders with a different mass ratio of WO_3 to Fe_3O_4 were synthesized via the chemical co-precipitation method. For each synthesis 50 mL of 0.14 mol L^{-1} $FeSO_4 \cdot 7H_2O$ aqueous solution and 100 mL 0.14 mol L^{-1} $FeCl_3 \cdot 6H_2O$ aqueous solution (molar ratio Fe^{2+} to Fe^{3+} = 1:2) were mixed in a double-walled vessel.

The mixture was stirred and warmed to 40 °C. Once this temperature was reached, the appropriate amount of WO_3 was added. After 30 min, NaOH was dropped into the mixture until the pH reached 6.8. A large amount of black precipitate was then generated. The suspension was stirred for 1 h and the obtained precipitates were filtered under vacuum and washed with double distilled water until no chloride was found in the filtrate (tested with $AgNO_3$). The particles were dried in a desiccator under vacuum with silica gel. Finally, the prepared composite particles were calcined at 370 °C (except for the materials used for the study of the effect of calcination temperature) for 3 h in static air.

By applying this procedure, four samples with WO_3 weight percent contents of 0.37, 1.41, 6.13 and 9.11%, w/w (denoted as $0.4WO_3/Fe_3O_4$, $1.4WO_3/Fe_3O_4$, $6.1WO_3/Fe_3O_4$ and

5

9.1WO_3/Fe_3O_4) were prepared. The same procedure, without the addition of WO_3, was used for the synthesis of pure Fe_3O_4. It should be noted that the Fe_3O_4 label does not mean that the only formed Fe species was magnetite (especially taking into account the calcination step during the sample preparation).

2.3. Characterization

The amount of WO_3 in the synthesized samples was determined by inductively coupled plasma–optical emission spectroscopy (ICP–OES) using a Thermo Scientific iCAP 6500 DuoICP spectrometer after microwave-assisted acid decomposition procedure.

The morphology of all samples was observed on a JEOL JSM−6460LV scanning electron microscopy (SEM) instrument.

Transmission electron microscopy (TEM) observations were carried out by JEOL JEM-1400 Plus with an acceleration voltage of 120 kV. Before TEM measurements, a suspension of 10 mg of sample in ethanol was prepared in a 50 mL volumetric flask and treated for 10 min in an ultrasonic bath. From the obtained dispersion, 5 μL were transferred on a holey carbon coated Cu grid. After drying at room temperature, the sample was used for measurement. High resolution transmission electron microscopy (HRTEM) and energy dispersive X-ray (EDX) mapping analysis were carried out by Talos F200X-FEI. The sample was prepared according to TEM procedure.

The X-ray powder diffraction (XRPD) measurements were performed on a Philips 1050 X-ray powder diffractometer using Ni-filtered Cu Kα radiation and Bragg–Brentano focusing geometry. The patterns were taken in the 10–70° 2θ range with a step of 0.05°and an exposure time of 6 s per step. Using the X-ray Line Profile Fitting Program (XFIT) with a Fundamental Parameters convolution approach to generating line profiles [35], the coherent domain sizes of the synthesized powders were calculated. Additional, XRPD measurements were conducted on Rigaku Smartlab X-ray Diffractometer in θ-θ geometry (the sample in horizontal position) in parafocusing Bragg-Brentano geometry using D/teX Ultra 250 strip detector in 1D XRF suppression mode with CuK$_{\alpha1,2}$ radiation source ($U = 40$ kV and $I = 30$ mA). The XRPD patterns were collected in 15−90° 2θ, with the step of 0.01°, and the data collection speed of 3 °/min. The low background single crystal silicon sample holder was used to minimize the background. The crystal phases were identified in dedicated Rigaku PDXL 2.0 software (with implemented ICCD PDF-2 2016 database).

Nitrogen adsorption-desorption isotherms were measured at −196 °C using an automated apparatus Sorptomatic 1990, Thermo Finningen. Before the adsorption, the samples were outgassed for 16 h at 110 °C under a residual pressure lower than 0.1 Pa.

6

The specific surface area of the samples, S_{BET}, was calculated according to the Brunauer, Emmet, Teller method, from the linear part of the nitrogen adsorption isotherms at relative pressure region determined according to Thommes at al. [36]. Micropore volumes (V_{mic}) were estimated according to the Dubinin–Radushkevich method [37]. Mesopore volume (V_{meso}) and pore size distribution were determined from the desorption branch of the isotherms using the Barrett–Joyner–Halenda [38] model with standard isotherm of Lecloux and Pirard [39] in the relative pressure region which corresponds solely to the mesoporous area (pore width 2−50 nm).

The UV-Vis diffuse reflectance spectra (UV-Vis DRS) were obtained by using a Nicolet Evolution 500 spectrophotometer equipped with a diffuse reflectance accessory, in the wavelength range of 250−800 nm using a SRS-99-010 Labsphere Spectralon as reference material.

The magnetic properties were investigated on a commercial SQUID-based Quantum Design XL-5 magnetometer equipped with a superconducting coil capable of producing magnetic fields in the range −5 T to +5 T. The field dependence of the isothermal magnetisation was measured at 27 °C and −268 °C. For low-temperature measurements, samples were cooled down in a zero magnetic field.

The efficiency of magnetic separation of photocatalyst from suspension was measured by a modified commercial spectrophotometer (CECIL Instruments Cambridge). This modification relates to a newly constructed holder for the samples, which allowed the presence/absence of a permanent magnet (Fig. S4). Cylindrical Pyrex tubes with an outer diameter of 24 mm and a wall thickness of 1.5 mm were used as sample containers. The separation efficiency for the studied materials was determined by measuring transparency at a wavelength of 480 nm. The magnet used had a magnetic field strength of 160 mT. The magnetic field strength was measured using a calibrated magnetometer (Sentron AG, CH-6300, ZUG). In all measurements, the material (0.05 g) was suspended in distilled water (30 mL). Subsequently, the slurry was intensively mixed, and after mixing was stopped, the transparency values were read at appropriate time intervals. For all studied materials, firstly, the separation efficiency was measured under the action of the gravitational field (GF, without magnet) and then under the magnetic field (MF). All measurements were carried out in triplicate.

2.4. Photocatalytic activity measurement

The catalytic efficiency of the prepared WO_3/Fe_3O_4 catalysts was studied in a batch reactor made of Pyrex glass (total volume cca. 100 mL, solution depth 46 mm). The UV radiation was provided by a 125 W high-pressure mercury lamp ($\lambda > 290$ nm, Philips HPL-N, emission bands in UV region at 304, 314, 335, and 366 nm, with the maximum emission at 366 nm) [40]. The intensity of UV radiation was $3.57 \cdot 10^{-3}$ W cm^{-2}. Irradiation with simulated sunlight (SS) radiation was performed using a set of four 35 W halogen lamps ($\lambda > 300$ nm, VITO, MR16), placed symmetrically around the reactor. The emission spectrum of the halogen lamps is illustrated in Fig. S2. UV and Vis radiation intensities for the applied SS radiation were $1.8 \cdot 10^{-4}$ W cm^{-2} and $116.2 \cdot 10^{-3}$ W cm^{-2}, respectively.

Appropriate amounts of WO_3/Fe_3O_4 and H_2O_2 were suspended in 30 mL of TCL aqueous solution (except for the study of direct photolysis), and the pH was adjusted by adding H_2SO_4 or NaOH. The suspension was stirred continuously in darkness for 15 min before irradiation so as to ensure equilibrium adsorption of TCL by the photocatalyst and to obtain a constant irradiation intensity output. The absence of adsorption of TCL on the photocatalyst was preliminarily checked by an experiment in the dark lasting 2 h.

Oxygen (99.99% purity) was continuously fed to the bottom of the reactor at a constant flow rate of 5 mL min^{-1}. Apart from oxygen bubbling, the solution was homogenised with the aid of a stirring bar, to ensure completely mixed batch conditions. Control experiments carried out under O_2 flow by stopping the irradiation showed that there were no losses of volatile compounds during degradation. The temperature of the reaction solution was kept at 25 ± 0.5 °C throughout the experiment by a water circulation system.

2.5. Analytical procedure

For the kinetic studies of TCL removal by liquid chromatography-diode array detection (HPLC-DAD), 0.5 mL aliquots of the reaction mixture were sampled at the beginning of the experiment and at various time intervals during irradiation, followed by filtration through a Millipore (Millex-GV, 0.22 μm) membrane filter. The absence of pesticide adsorption onto the filter was confirmed by preliminary testing.

Measurements were carried out on a Shimadzu 20A series ultra-fast liquid chromatograph (UFLC, Shimadzu Cooperation), equipped with a ZorbaxEclypse XDB-C18 (150 mm × 4.6 mm i.d., particle size 5 μm) column. The injection volume was 20 μL. The column temperature was held at 25 °C, the eluent was a mixed solution of 0.1% H_3PO_4–ACN (7 : 3, v/v), pH 2.56, and the total flow rate was 1.0 mL min^{-1}. TCL elution was monitored at 242 nm (absorption maximum for TCL), with a retention time of 5.84 min.

8

pH measurements were made using a Hanna Instruments combined glass electrode (Kehl, Germany), on a previously calibrated pH-meter (Iskra, Kranj, Slovenia).

The radiation energy fluxes were measured using a Delta Ohm HD 2102.2 (Padova, Italy) radiometer which was fitted with the LP 471 UV (spectral range 315–400 nm) and LP 471 RAD (spectral range 400–1050 nm) sensors.

3. Results and discussion

3.1. Structural characteristics

3.1.1. SEM and TEM analysis of WO_3/Fe_3O_4 catalysts

In addition to the starting WO_3 and the synthesized catalysts, an SEM micrograph of Fe_3O_4 is also shown in Fig. 1. The difference in the morphology of Fe_3O_4 (unmodified support, Fig. 1a) and WO_3 samples (Fig. 1b) is quite obvious. In contrast, differences between pure Fe_3O_4 and the synthesized catalysts are almost unobservable (Fig. 1c–f). The SEM images of the synthesized catalysts indicate that the particles form clusters of irregular shapes whose size varies between 20 and 40 nm. The WO_3 particles were substantially larger in size and shape, 60–700 nm.

The cloudy form of irregular shapes is characteristic for Fe_3O_4 support, as well as for all photocatalysts. The separation of WO_3 species on Fe_3O_4 support is not recognisable even in the micrography of the sample with the greatest amount of WO_3 ($9.1WO_3/Fe_3O_4$).
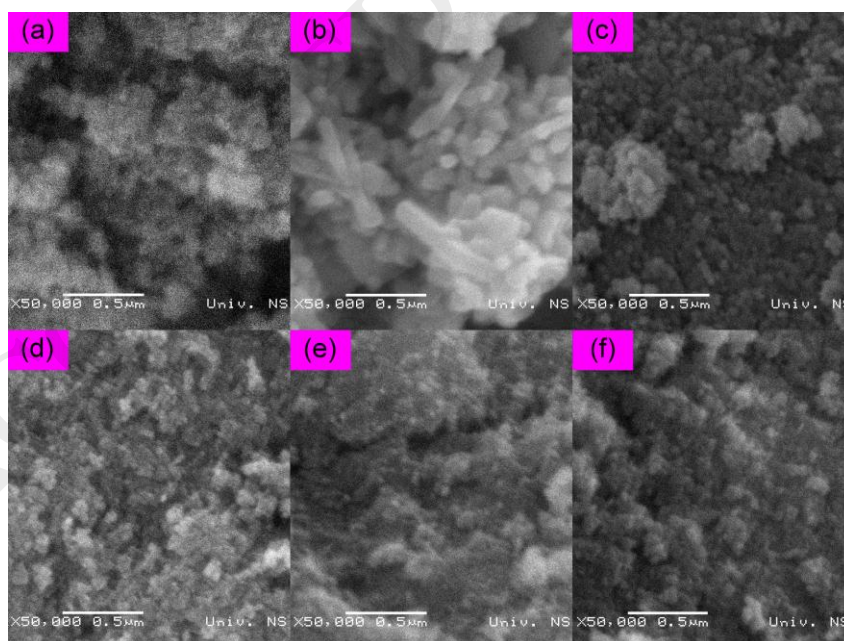

Fig. 1. SEM images: (a) unmodified Fe_3O_4 and (b) unsupported WO_3 species. Synthesized nanopowders:
(c) $0.4WO_3/Fe_3O_4$; (d) $1.4WO_3/Fe_3O_4$; (e) $6.1WO_3/Fe_3O_4$ and (f) $9.1WO_3/Fe_3O_4$. Line bar 0.5 μm.

The TEM micrograph of calcinated unmodified Fe_3O_4 (Fig. 2a) indicates its complex composition. Individual domains, that build an almost mosaic structure are clearly visible, and the smallest recognizable ones do not exceed 8 nm along the longest axis. On the other hand, on the WO_3 micrograph (Fig. 2b), a lot of rods or prismatic like structures that reach lengths up to 75 nm can be seen.

Many spheroidal structures of very different dimensions, ranging from just several nanometres to over 250 nm, can be found on the micrography of sample $6.1WO_3/Fe_3O_4$ (Fig. 2c). Although a certain mosaic structure is visible, especially on the particles marked by arrows, it is almost impossible to spot the building units of similar morphology that exist in Fig. 2a and b. This suggests that the applied procedure of photocatalyst synthesis does not simply deposit Fe species on WO_3.
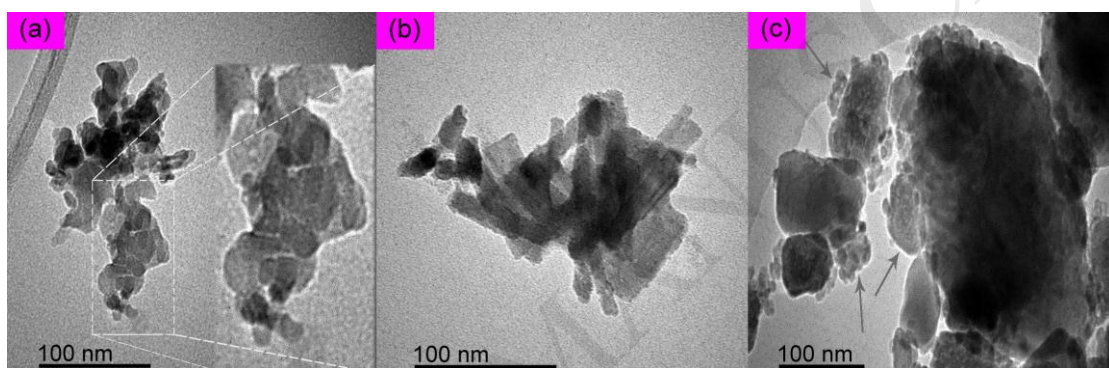

Fig. 2. TEM images of: (a) unmodified Fe_3O_4, (b) unsupported WO_3 species, and synthesized nanopowder $6.1WO_3/Fe_3O_4$. Line bar 100 nm.

The TEM-EDX analysis of the $6.1WO_3/Fe_3O_4$ photocatalyst confirmed the presence of Fe, O and W (Fig. 3). Although in the presence of W there was some non-homogeneity (more intensively green coloured regions in the Fig. 3), its presence in the overall area of the $6.1WO_3/Fe_3O_4$ aggregate was noticeable.

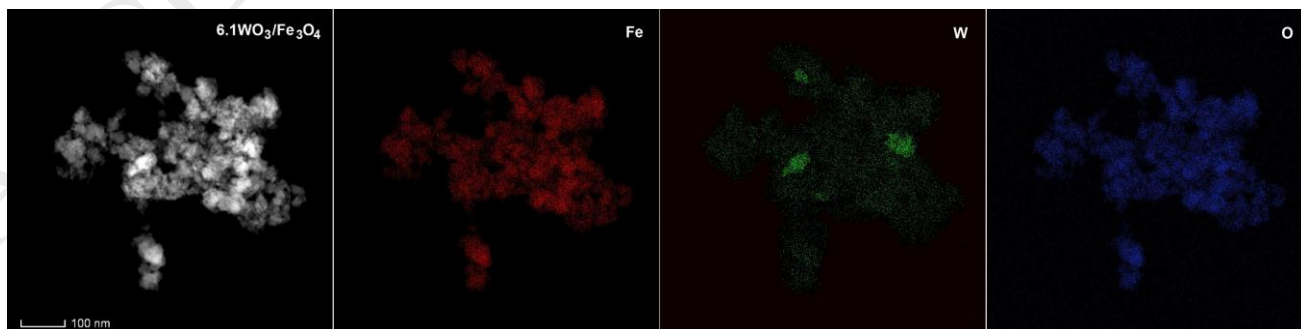**Fig. 3.** TEM and EDX mapping analysis of $6.1WO_3/Fe_3O_4$ photocatalyst.

3.1.2. Textural properties

10

Fig. 4 contains nitrogen adsorption/desorption isotherms of the four synthesized catalysts, as well as isotherms of unmodified Fe_3O_4 and unsupported WO_3, while the corresponding calculated textural parameters are given in Table 1.

The isotherm of unsupported WO_3 belongs to type II which is characteristic for non-porous and macroporous materials [36]. Although it is difficult to distinguish between these two groups of materials by N_2 physisorption measurements alone, the small specific surface area and the negligible content of the micro- and mesopores volume, as well as the results of the SEM measurements, indicate the non-porous property of the synthesized WO_3.
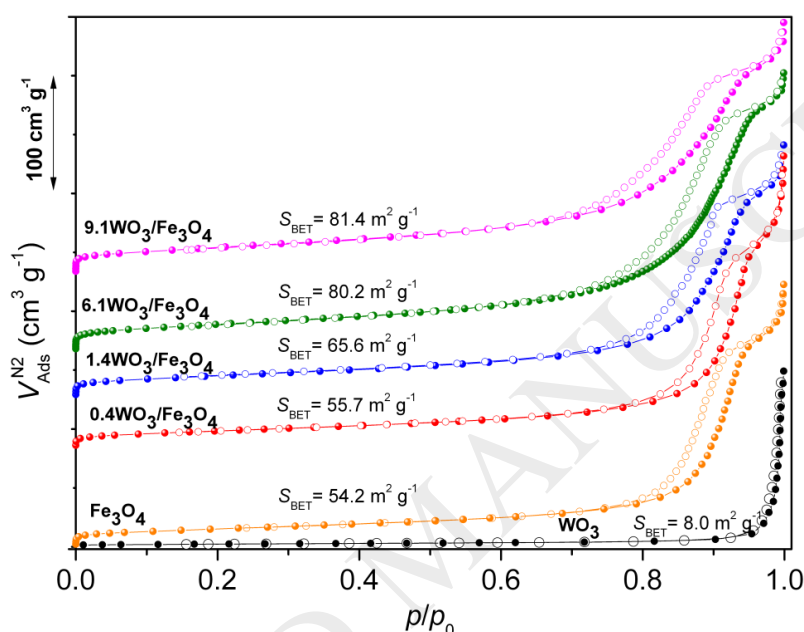

Fig. 4. Nitrogen isotherms at −196 °C of unsupported WO_3, unmodified Fe_3O_4 and WO_3/Fe_3O_4 catalysts (adsorption - filled symbols; desorption - empty symbols).

It should be noted that the values of the specific surface area (S_{BET}) determined by the nitrogen physisorption at -196 °C, do not necessarily represent the specific surface area of the material. The inability of N_2 to fill the ultramicropores present in the hexagonal WO_3 (h-WO_3) structure was demonstrated by Sun et al. [41]. They reported measured S_{BET} values (applying N_2 at −196 °C) of h-WO_3 that is practically identical to the S_{BET} value of the WO_3 sample presented in this work (8.1 vs 8.0 m^2 g^{-1}), and differ significantly from the S_{BET} of monoclinic WO_3 structure (5.7 $m^2 g^{-1}$). Thus, the results of Sun et al. [41] suggest that our applied synthesis procedure lead to the formation of hexagonal WO_3 structure.

Table 1. Results of N_2 physisorption and XRD measurements

S_{BET},	V_{meso},	V_{mic},	$^aD_{max}$,	Crystallite size, nm		$^bHem/Mag$

	$m^2\,g^{-1}$	$cm^3\,g^{-1}$	$cm^3\,g^{-1}$	nm	Hematite	Magnetite	ratio
Fe_3O_4	54.2	0.281	0.021	18.1	10.4	13.8	9.2
$0.4WO_3/Fe_3O_4$	55.7	0.257	0.019	19.5	10.7	12.3	4.6
$1.4WO_3/Fe_3O_4$	65.6	0.278	0.022	14.6	14.2	13.2	1.8
$6.1WO_3/Fe_3O_4$	80.2	0.332	0.026	14.0	6.4	14.9	0.2
$9.1WO_3/Fe_3O_4$	81.4	0.283	0.026	9.4	6.6	12.8	0.4
WO_3	8.0	0.014	0.003	-	-	-	

[a]D_{max} maximum pore width; [b]Hematite to magnetite ratio

The positive slope across much of the relative pressure range, the indication of a plateau in the region of high relative pressure, and the existence of a hysteresis loop associated with the filling/emptying of pores phenomena, all point out the mesoporous nature of the unmodified Fe_3O_4 and all the synthesized catalysts, classifying the obtained isotherms as Type IV according to IUPAC [36]. Although the shapes of all the isotherms and their hysteresis loops are similar, some differences can be seen on the slope and position on the desorption branches. This indicates a particular difference in the mesopore region of the analysed samples.

Indeed, the results in Table 1 and pore size distribution (Fig. S3) show that the values of textural parameters are changed by the addition of WO_3. This applies in particular to the maximum pore width (D_{max}), which decreases from 18.1 nm for unmodified Fe_3O_4 to 9.4 nm for the catalyst with the highest content of WO_3. The high value of D_{max} is significant because it ensures the absence of diffusion limitation during photodegradation process (which is even the case for the catalyst with the highest content of WO_3).

The apparent increase in S_{BET} caused by the addition of WO_3 (despite its small specific surface area) can have a chemical or physical origin. Chemical origin implies the creation of a new phase (or phases) caused by the chemical interaction of the WO_3 added to the present Fe-types. Physical origin implies changing the crystallization mechanism of Fe-species due to the existence of numerous crystallization centres that originates from WO_3, with a possible change in Fe-species ratio present in the unmodified Fe_3O_4. In principle, the chemical or physical origins do not exclude each other, nor do they eliminate the increase in the amount of amorphous phase(s).

3.1.3. XRD measurements of WO_3/Fe_3O_4 catalysts

The XRD patterns of the synthesized catalysts, unmodified Fe_3O_4 and unsupported WO_3 are shown in Fig. 5. The calculated crystallite sizes of phases identified in the catalysts, as well as the phase ratios, are given in Table 1.
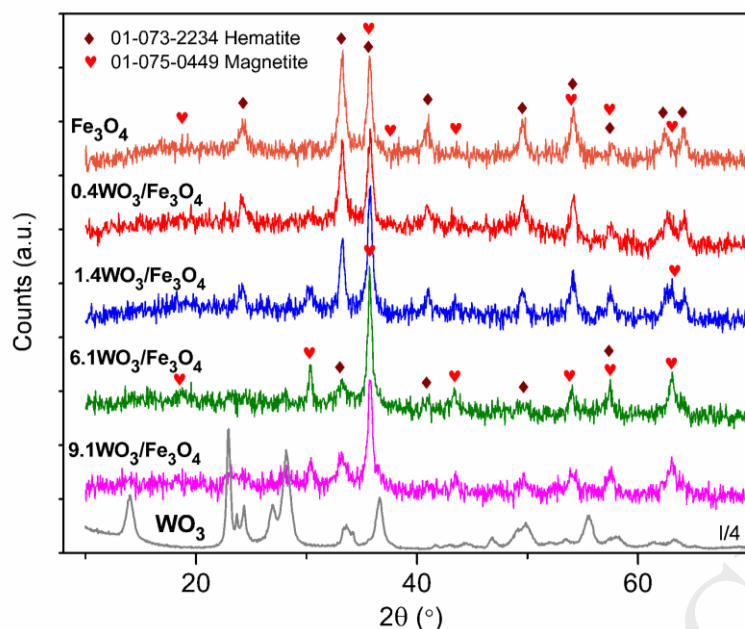
Fig. 5. XRD pattern of unsupported WO_3, unmodified Fe_3O_4 and WO_3/Fe_3O_4 catalysts.

For the sake of comparison, the signal of the unsupported WO_3 shown in Fig. 5 has been reduced in intensity four times in relation to the original values, and corresponds to the hexagonal WO_3 identified by Marques at al. (ICDD 01-075-2187) [42]. These authors synthesized hexagonal WO_3 nanoparticles from aqueous solutions of $Na_2WO_4 \cdot 2H_2O$ and Na_2SO_4 at pH = 1.8, whereas with the same synthesis procedure at pH = 0.0 and 0.4, they obtained monoclinic WO_3 and orthorhombic $WO_3 \cdot 0.33H_2O$ species respectively.

The crystallite size of the obtained unsupported h-WO_3 is 9.2 nm. The presence of any WO_3 phases cannot be identified on the diffractograms of the WO_3/Fe_3O_4 catalysts containing the two lowest WO_3 concentrations. Furthermore, there is no evidence of an increase in amorphisation in the diffractograms of the WO_3/Fe_3O_4 catalysts synthesized, as a result of WO_3 modification.

The barely visible peak at $2\theta \approx 28.15°$ is the only evidence of the presence of WO_3 phase in the catalysts with a higher tungsten concentration (6.1 and 9.1% WO_3). This could indicate a high irregularity of the WO_3 phase in the synthesized WO_3/Fe_3O_4 catalysts, although the possibility of the presence of the tungsten in another phase cannot be ruled out.

Using the same synthesis procedure to produce unmodified Fe-oxide material (without WO_3) results in the presence of two Fe-oxide phases: hematite (α-Fe_2O_3) and magnetite (Fe_3O_4), in a 9.2 to 1 ratio. Despite the appropriate 1:2 molar ratio of $Fe^{2+}:Fe^{+3}$ used in the synthesis process to obtain magnetite, the content of Fe_3O_4 in the final product is relatively small (less than 10%). This is most likely due to the synthesis being carried out under an air

13

atmosphere. Given the last stage of the synthesis (calcination at 370 °C, for 3 h in the presence of oxygen from the air), a phase transition from Fe_3O_4 to Fe_2O_3 is very plausible [43,44], especially when taking into account the small crystallite dimension of the obtained magnetite [45].

The influence of tungsten addition on the Fe-oxide phase ratio (α-Fe_2O_3 to Fe_3O_4) is a particularly interesting result of this study. Introducing even the smallest amount of tungsten significantly increases the amount of magnetite produced, with a corresponding drop in the hematite content. The highest concentration of magnetite, almost 80%, is found in the sample with 6.1% WO_3. This corresponds to an 8-fold increase of Fe_3O_4 compared to its content in the unmodified Fe-oxide substance.

The crystallite size of the Fe_3O_4 in the catalysts does not change significantly and is around 13 nm, except for the $6.1WO_3/Fe_3O$ catalyst which has a dimension of about 15 nm. At the same time, a significant drop in the crystallite size of the hematite phase can be seen in the two catalysts with greater WO_3 contents.

Additionally, results of XRPD measurements and identification (Rigaku Smartlab X-ray Diffractometer in θ-θ geometry) are shown in Figs. S4-S6. It can be seen that the only difference with the results of XRDP measurements previously presented in the manuscript was a slightly better signal to noise ratio obtained by subsequent measurements. In the $6.1WO_3/Fe_3O_4$ photocatalyst diffractogram, the presence of hexagonal WO_3 was confirmed (Figs. S4 and S6), and also the presence of both iron phases hematite Fe_2O_3 and magnetite Fe_3O_4.

By analyzing the micrographs obtained from the HRTEM measurements, the interplanar distance values (Fig. S7 and Table S1) were determined. The calculated values are compared with those listed in ICCD cards. The close values for interplanar distance obtained by comparison (Table S1) confirm the justification of the proposed phase composition of the $6.1WO_3/Fe_3O_4$ photocatalyst.

Overall the results of XRD, SEM and TEM measurements showed that the applied procedure resulted in well-dispersed WO_3 species on mixed Fe-oxide (Fe_3O_4-Fe_2O_3).

As far as we know, there is no data in the literature about the possibility of controlling the Fe_2O_3 to Fe_3O_4 phase ratio using W or WO_3. Upcoming research should provide us with further insight into the full potential of this approach in phase ratio control, especially taking into account the effects of different synthetic parameters (e.g. wider molar ratio of WO_3 to Fe-oxide species, temperature and time of calcination, and atmospheric composition during calcination).

14

3.1.4. Magnetic characterization

The results of the magnetic properties of unmodified Fe_3O_4 and WO_3/Fe_3O_4 catalysts measured at -268 °C (saturation magnetisation - Ms; remanent magnetisation - Mr; coercive field from descending - Hc- and ascending - Hc+ branches) are given in Table 2. In additional, hysteresis curves of the same materials measured at 27 °C are presented in Fig. 6. Each curve contains the corresponding saturation magnetisation values.

Table 2. Characteristic parameters from magnetic hysteresis measurements at −268 °C for unmodified Fe_3O_4 and WO_3/Fe_3O_4 catalysts

	Ms, emu g^{-1}	Mr, emu g^{-1}	Hc-, Oe	Hc+, Oe
Fe_3O_4	5.4	1.7	−465	396
$0.4WO_3/Fe_3O_4$	18.6	6.1	−412	334
$1.6WO_3/Fe_3O_4$	23.9	6.9	−362	301
$6.1WO_3/Fe_3O_4$	43.2	11.9	−283	252
$9.1WO_3/Fe_3O_4$	35.8	9.9	−305	271

Although a hysteresis loop exists for all samples for the measurements at −268 °C, the quadrants of Fig. 6 only show the hysteresis loop of the unmodified Fe_3O_4. The insert in the fourth quadrant shows part of the loop in the low field region, with values of Mr, Hc- and Hc+, for the same sample. The hysteresis loop of the unmodified Fe_3O_4 sample was selected for presentation because the loop for this sample is the widest (i.e. the descending and ascending branches deviate the most from reversibility).
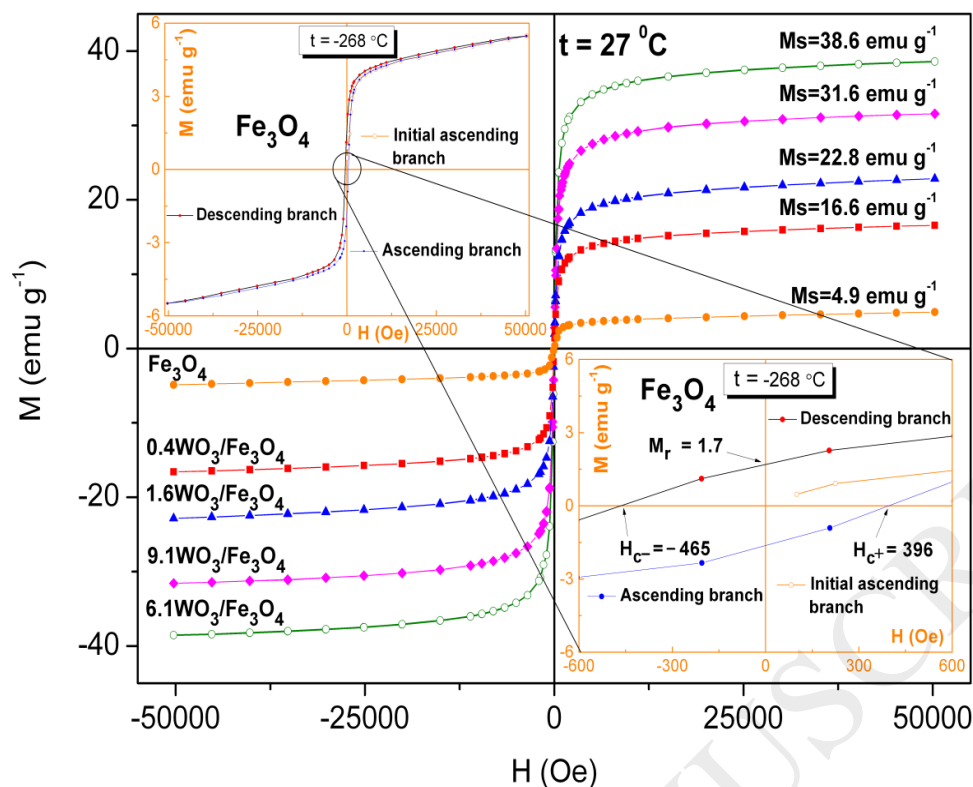
15

Fig. 6. First and third quadrant - hysteresis loop measured at 27 °C for the catalysts and Fe_3O_4 unmodified with WO_3; Second quadrant - hysteresis loop curve of Fe_3O_4 measured at −268 °C; Fourth quadrant - low field region with values of Mr, Hc- and Hc+ (units omitted).

The saturation magnetisation value (Table 2) is the smallest for the sample unmodified with WO_3 (5.4 emu g^{-1}). The significantly lower Ms value of this sample compared to the values given for the bulk magnetite material [46] reflects the amount of magnetite phase present in the sample. The influences of crystallite and the particle size of magnetite, its morphology and texture, as well as the presence of a hematite phase (antiferromagnetic material below the Morin transition at −23 °C, and a canted antiferromagnetic or weakly ferromagnetic above Morin transition and below Néel temperature) are well documented in the literature [47−52].

For all the samples, the magnetic saturation value is lower for measurements carried out at the higher temperature with complete reversibility of the hysteresis curve. The value of saturation magnetisation represents complete alignment of the magnetic field vector in the direction of the outer magnetic field. Therefore, the decrease in the value of Ms with increasing temperature is caused by the inability of magnetic moments to align, due to the effect of increasing heat energy. For all measurements at a temperature of −268 °C, the values of Hc- and Hc+ are the highest, while the remanent magnetisation is the lowest, for the unmodified Fe_3O_4 sample.

16

The lowest value of Hc- and Hc+ was observed for sample 6.1WO$_3$/Fe$_3$O$_4$, while the values of saturation magnetisation and remanent magnetisation are the highest for this sample. This result can be explained by the highest magnetite phase content in sample 6.1WO$_3$/Fe$_3$O$_4$, particularly if the crystallite dimensions of magnetite phase present in all samples (based on XRD measurements) are approximately the same.

The results obtained by the magnetic measurements not only confirm the magnetic nature of the synthesized materials but also point to potential differences in their behaviour during separation from the working solution of the suspension.

3.1.5. UV-Vis DRS of WO₃/Fe₃O₄ catalysts

In addition to chemical composition, morphological and structural properties, for the catalytic application of the materials, their optical properties are significant, primarily absorption in the UV-Vis range of the electromagnetic spectrum. Therefore, DRS measurements were performed in the UV-Vis region.

From the obtained DRS spectra (Fig. 7) it follows that the absorption of the synthesized catalysts in the observed wavelength range was similar to that obtained for unmodified Fe$_3$O$_4$ and significantly higher than WO$_3$. It can be concluded that an efficient charge carrier separation for the synthesized catalysts can be achieved using SS radiation. Comparing the reflectances at 752 nm, it can be noticed that the 6.1WO$_3$/Fe$_3$O$_4$ catalyst showed the highest absorption, and therefore it could be expected to show the highest degradation efficiency.
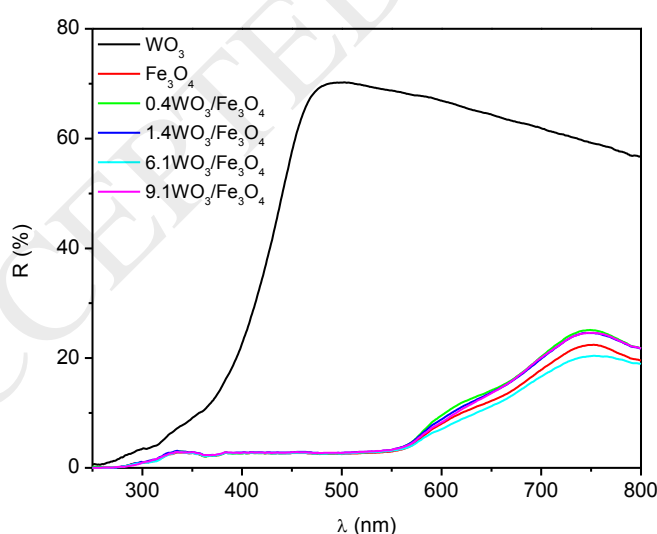

Fig. 7. UV-Vis DRS of unsupported WO₃, unmodified Fe₃O₄ and WO₃/Fe₃O₄ catalysts.

3.2. UV photodegradation studies

17

3.2.1. Effect of WO$_3$ content in WO$_3$/Fe$_3$O$_4$ catalyst

By applying various AOPs under the influence of UV radiation, it has been observed that TLC is susceptible to degradation, with the highest degradation efficiency determined using the Fe$_3$O$_4$/H$_2$O$_2$ system (Fig. 8). For this system, the degradation efficiency was 93.7% after 2 h of irradiation. Furthermore, the efficiency of semiconductor catalysis with Fe$_3$O$_4$ was significantly improved by indirect photolysis. As can be seen from Fig. 8, in the presence of H$_2$O$_2$ alone, just 73.8% of TLC was degraded in the same irradiation period. Note that hydrogen peroxide can contribute to overall efficiency both as an electron scavenger, and also as a component of the photo-Fenton process [53].

An experiment with unsupported WO$_3$ was also conducted to examine its contribution to overall degradation efficiency. Unsupported WO$_3$ was added at a substantially higher mass concentration (67 mg L^{-1}) than the amount present in 0.42 g L^{-1} of 9.1WO$_3$/Fe$_3$O$_4$ (38 mg L^{-1}), but the reduced efficiency of the WO$_3$/H$_2$O$_2$ system can be explained by the still significantly lower initial mass concentration of WO$_3$ (67 mg L^{-1}) compared to that of the other materials used (0.42 g L^{-1}). For the studied materials, in the presence of H$_2$O$_2$ and UV radiation (Fig. 8), it can be concluded that increasing the WO$_3$ content leads to a decrease in degradation efficiency in the sequence 0.4WO$_3$/Fe$_3$O$_4$ (91.3%) > 1.4WO$_3$/Fe$_3$O$_4$ (85.6%) > 6.1WO$_3$/Fe$_3$O$_4$ (83.8%) > 9.1WO$_3$/Fe$_3$O$_4$ (63.4%).
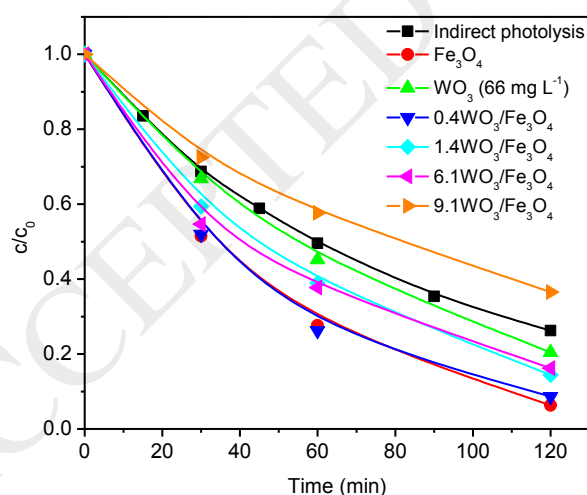

Fig. 8. Effect of WO$_3$ content in WO$_3$/Fe$_3$O$_4$ on the kinetics of TCL photodegradation in the presence of UV radiation. Operating conditions: [TCL]$_0$ = 0.38 mM, [H$_2$O$_2$]$_0$ = 45 mM, photocatalysts = 0.42 g L^{-1} and pH = 2.8.

3.2.2. Effect of dosage of 6.1WO$_3$/Fe$_3$O$_4$ catalyst

18

The effect of catalyst loading on the degradation efficiency of TCL was investigated keeping all other experimental parameters constant, and the results are shown in Fig. 9. The effect was tested for $6.1WO_3/Fe_3O_4$ loading in the range from 0.21 to 1.67 g L^{-1} (Fig. 9a). A steady increase in the degradation efficiency up to 0.42 g L^{-1} of catalyst was observed, with a subsequent reduction in efficiency (Fig. 9b). The increase of catalyst loading from 0.21 to 0.42 g L^{-1} enhanced degradation efficiency due to the increase in the catalyst surface area, which enhances the absorption of photons. The degradation efficiency decrease at loading above the optimum value of 0.42 g L^{-1} can be explained by the reduced penetration of radiation and deactivation of activated molecules due to collision with the ground-state molecules [54]. Accordingly, the overall number of photons that can be reached by the catalyst particles and the production of $^{•}OH$ radicals both decreased with the greater loading of the catalyst. Further, at higher catalyst loading it is difficult to maintain a homogeneous suspension due to particle agglomeration which decreases the number of active sites [55].
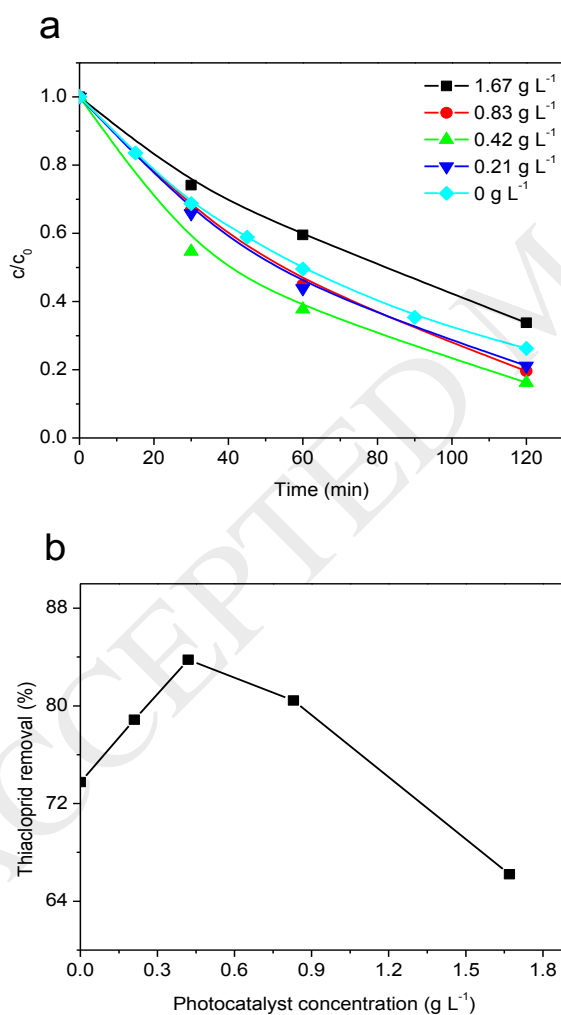

Fig. 9. Effect of $6.1WO_3/Fe_3O_4$ loading on the kinetics of TCL photodegradation (a) and degradation efficiency after 120 min of UV irradiation (b). Operating conditions: $[TCL]_0 = 0.38$ mM, $[H_2O_2]_0 = 45$ mM and pH = 2.8.

3.2.3. Effect of calcination temperature

Calcination temperature has a very important influence on the optical properties, crystal size, and crystal structure of the prepared photocatalyst [56]. Hence, $0.4WO_3/Fe_3O_4$ catalyst was calcined at 100, 200, 300, 370, and 500 °C, and results of the subsequent degradation efficiency are shown in Fig. 10. It was found that TCL degradation efficiency decreases by 15% when the calcination temperature increases from 100 to 300 °C, followed by an increase in decomposition efficiency by 21% with an increase in temperature to 370 °C (Fig. 10b). Further increases in calcination temperature did not lead to significant changes in the efficiency of TCL degradation.
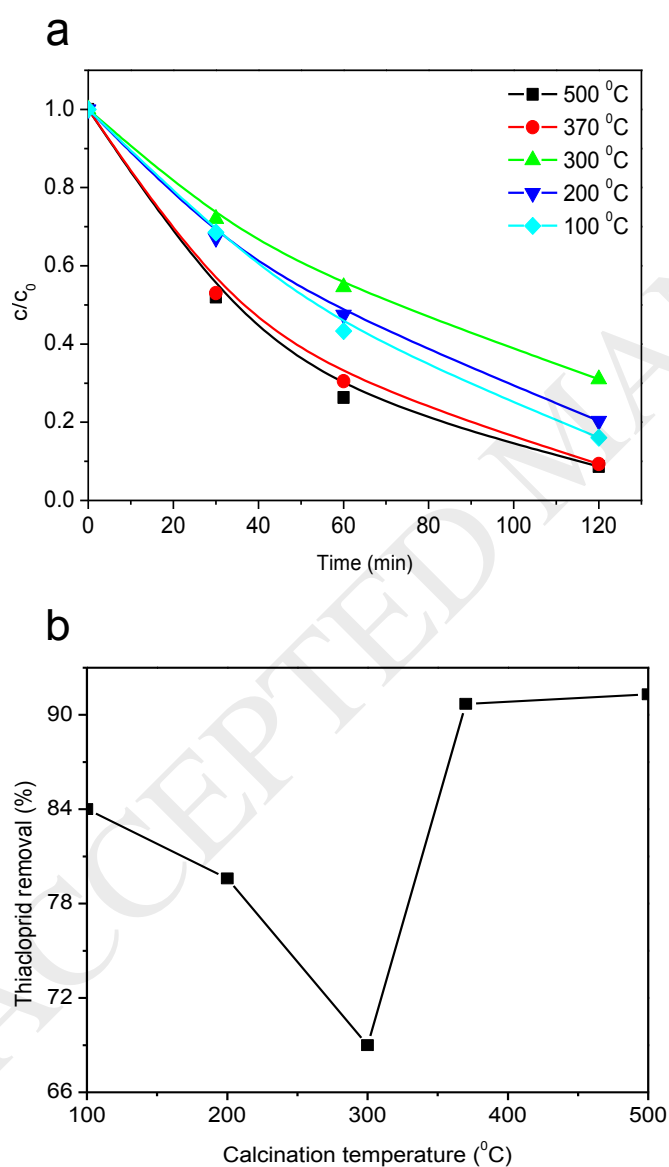
Fig. 10. Effect of the calcination temperature of $0.4WO_3/Fe_3O_4$ on the kinetics of TCL photodegradation (a) and degradation efficiency after 120 min of UV irradiation (b). Operating conditions: $[TCL]_0 = 0.38$ mM, $[H_2O_2]_0 = 45$ mM, $0.4WO_3/Fe_3O_4 = 0.42$ g L^{-1} and pH = 2.8.

20

3.3. Simulated sunlight photodegradation studies

3.3.1. Effect of WO₃ content in WO₃/Fe₃O₄ catalyst

Bearing in mind the significant potential application of the photo-Fenton process using solar radiation, further tests were conducted to examine the performance of different AOPs through degradation of TCL under SS radiation. This light source ensures degradation proceeds similarly to a practical application under sunlight. Based on the results shown in Fig. 11, it can be concluded that all the applied AOPs under the influence of SS radiation lead to TCL photodegradation.
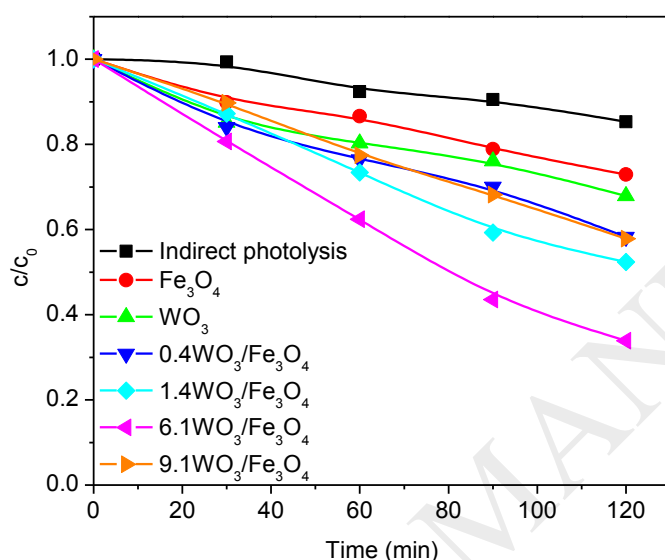

Fig. 11. Effect of WO_3 content in WO_3/Fe_3O_4 on the kinetics of TCL photodegradation in the presence of SS radiation. Operating conditions: $[TCL]_0 = 0.38$ mM, $[H_2O_2]_0 = 45$ mM, photocatalysts $= 0.42$ g L^{-1} and pH $= 2.8$.

Comparing the results obtained under SS radiation (Fig. 11) with those obtained for the same processes carried out in the presence of UV radiation (Fig. 8), in all cases a reduced efficiency was observed. However, in comparison with pure WO_3 and Fe_3O_4, all synthesized WO_3/Fe_3O_4 catalysts showed a higher efficiency. From all of the tested WO_3/Fe_3O_4 catalysts, $6.1WO_3/Fe_3O_4$ catalyst showed the highest photocatalytic efficiency (66.1% TCL was removed after 120 min of irradiation). This is in accordance with the obtained DRS spectra, based on which it is assumed that this catalyst exhibits photocatalytic activity in the visible part of the electromagnetic spectrum. Experimental results also indicate that the overall efficiency of photocatalytic degradation in the presence of SS radiation is the result of the heterogeneous photo-Fenton process [57,58], as well as of the coupling effect of the semiconductors WO_3 and Fe_3O_4 [59,60]. To examine which of these effects is dominant,

additional experiments were performed (Fig. 12). In the presence of SS radiation, the use of a heterogeneous photo-Fenton system that includes $6.1WO_3/Fe_3O_4/H_2O_2$ resulted in a 2.2 times higher degradation efficiency compared with the unmodified Fe_3O_4/H_2O_2 system. From these results, it can be concluded that besides the influence of the heterogeneous photo-Fenton process on the degradation efficiency, the coupling effect of the semiconductor also has a significant influence.
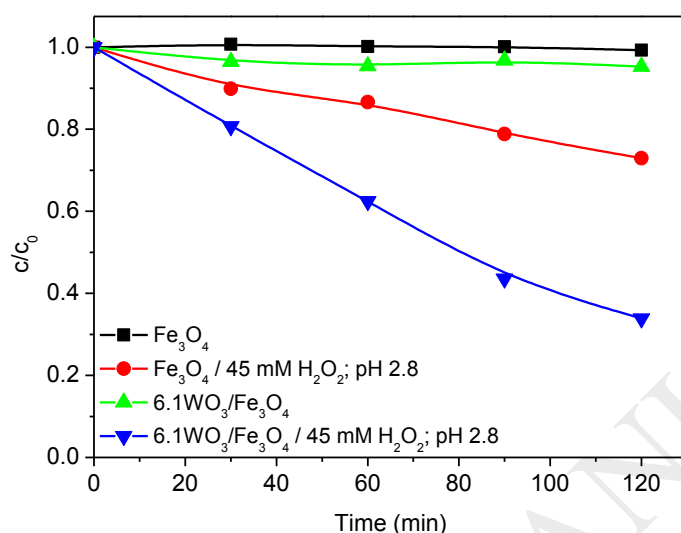

Fig. 12. Effect of the synergistic and heterogeneous photo-Fenton process of the catalyst on the kinetics of TCL photodegradation in the presence of SS radiation. Operating conditions: $[TCL]_0 = 0.38$ mM, photocatalysts $= 0.42$ g L^{-1}.

3.3.2. Effect of initial H_2O_2 concentration

As can be seen from Fig. 13, the initial H_2O_2 concentration is an important parameter for the efficiency of the $6.1WO_3/Fe_3O_4$ catalyst. However, increasing the amount of H_2O_2 added did not result in a linear increase in the efficacy of TCL photodegradation (Fig. 13b). While a rapid increase in the efficacy occurred at H_2O_2 concentrations from 0 to 22.5 mmol L^{-1} (62% of the TCL was degraded after 120 min of irradiation), in the concentration range of 45–67.5 mmol L^{-1} only a slight increase was observed (8.6%) (Fig. 13b). This behaviour can be explained by the fact that the higher concentrations of H_2O_2 result in a higher steady-state $^{\bullet}OH$ concentration and degradation efficiency of TCL [61]. Furthermore, H_2O_2 can increase the regeneration of Fe(III) from Fe(II) via photo-Fenton reduction and consequently increase the formation of $^{\bullet}OH$ radicals [62]. On the other hand, at higher concentrations, H_2O_2 also acts as an $^{\bullet}OH$ scavenger, producing the much less reactive hydroperoxyl radical ($HO_2^{\bullet}$), whereby less $^{\bullet}OH$ is available for TCL removal [61].
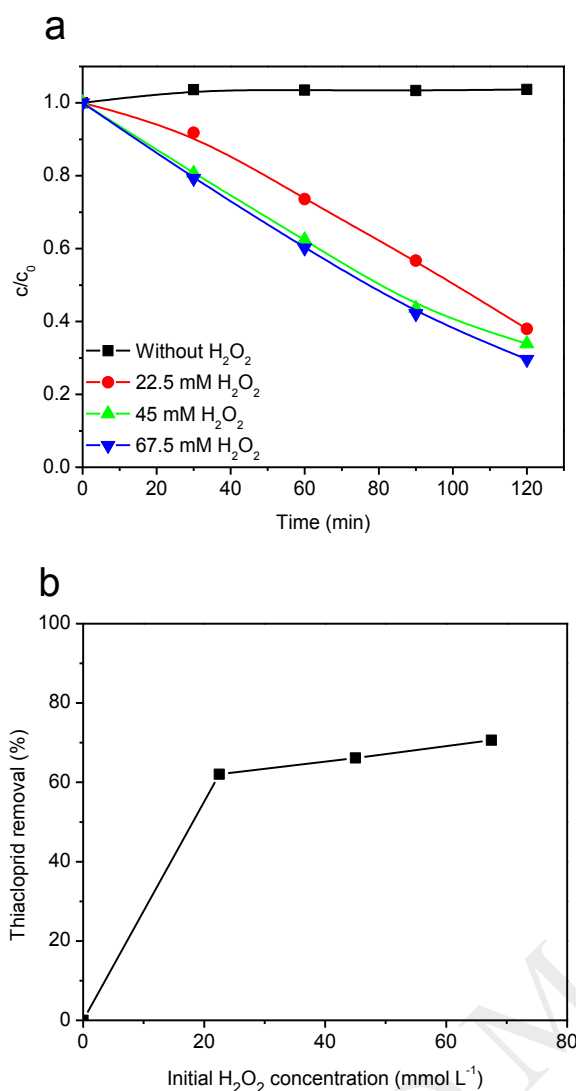
22

a

b

Fig. 13. Effect of initial H_2O_2 concentration on the kinetics of TCL photodegradation (a) and degradation efficiency after 120 min of SS irradiation (b). Operating conditions: $[TCL]_0 = 0.38$ mM, $6.1WO_3/Fe_3O_4 = 0.42$ g L^{-1} and pH = 2.8.

3.4. Synergistic effect in the photocatalytic degradation with WO_3/Fe_3O_4

Research into the fabrication of heterostructured semiconductor phase-junctions has recently been very active because of their high effectiveness in promoting the separation of photogenerated charge carriers and improving photocatalysis properties, especially regarding the utilization of visible light. Heterostructured photocatalysts with direct contact between p-type and n-type semiconductors have received broad attention because the large potential gradient and built-in electron field established at the junction level can induce efficient charge separation [63–65].

In iron oxide–semiconductor systems, iron oxides can be narrow band gap semiconductors, with a band gap value for Fe_2O_3 of 2.2 eV, and they can also absorb visible light. For example, the work function (ϕ) of α-Fe_2O_3 is 5.88 eV, which is higher than the

23

most common wide band gap semiconductors (TiO_2 is 3.87 eV, ZnO is 4.35 eV, SnO_2 is 4.3 eV, WO_3 is 5.24 eV, etc.) [66]. As shown in Fig. 14, the band configuration and photogenerated charge carrier separation at the interface of iron oxide–tungsten trioxide (wide band gap) under SS radiation is proposed. Under SS radiation, the photoinduced electrons and holes are separated at the interface of the iron oxide–tungsten trioxide. The photoinduced electrons in the CB of iron oxide tend to transfer to the CB of the tungsten trioxide due to the decreased potential energy, and hence the coupling structure reduces the electron-hole recombination probability and increases electron mobility. Thereby the electrons and holes are transferred to the surface of the iron oxide and tungsten trioxide, respectively, and finally form the most powerful and nonselective $^\bullet OH$ radicals, which can damage all types of organic/biomolecules. Super oxygen radical anions ($^\bullet O_2^-$) are formed by the combination of electrons with O_2 adsorbed on the surface of the semiconductor. An active species trapping test shows that $^\bullet O_2^-$ and $^\bullet OH$ are the main reactive species and take crucial roles in the photocatalytic oxidation reaction regardless of the light source [67,68].

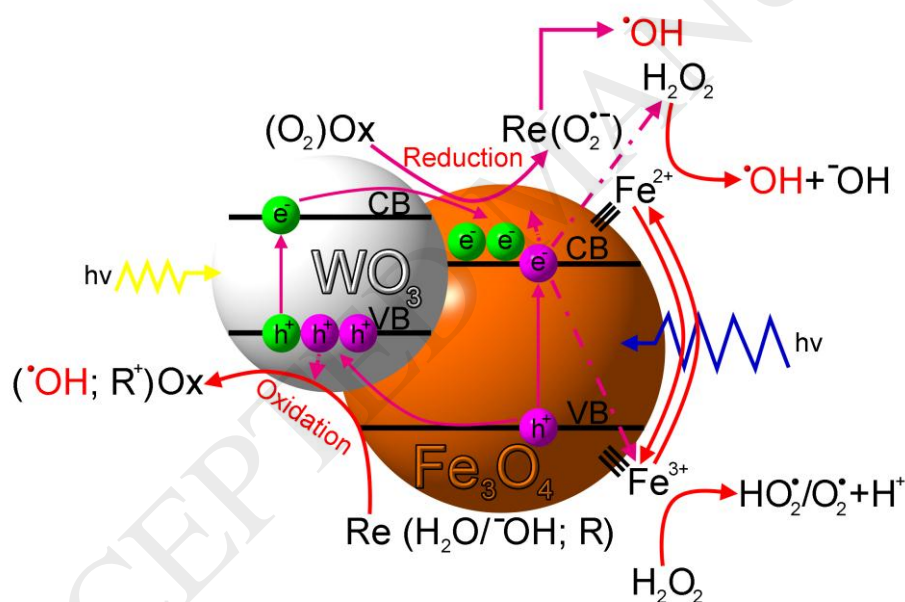**Fig. 14.** The charge-transfer process in the WO_3/Fe_3O_4 photocatalyst. After photon excitation by radiation, photogenerated electrons (e^-) and holes (h^+) migrate to Fe_3O_4 and WO_3, respectively, and react with the adsorbed species.

Further increases in process efficiency can be attributed to the H_2O_2 decomposition on the iron oxide surface which leads to the formation of larger amounts of radicals (surface heterogeneous photo-Fenton process) [69]. Also, the beneficial effect of the presence of Fe^{3+} species on the photocatalytic activity is due to the role of Fe^{3+} species acting as h^+/e^- traps, thus hindering the recombination rate and enhancing the photocatalytic activity. This benefit

24

in the photodegradation efficiency arises from the surface photoreduction of Fe^{3+} to Fe^{2+}, which produces new radicals in the reaction with H_2O_2 [69].

In our case, using UV radiation (Fig. 8), the main route of radical generation was the photolysis of H_2O_2 [29]. The presence of WO_3 in the photocatalysts had a negative effect on this pathway of radicals generation. On the other hand, in the experiments performed in the presence of SS radiation (Fig. 11), it can be seen that indirect photolysis had a significantly smaller effect on the overall efficiency of photodegradation, and that the other paths shown in Fig. 14 become dominant in generating radicals; it can also be seen that the presence of WO_3 in certain concentrations positively affects the efficiency of photodegradation.

3.5. Magnetic separation process

Since the ability to readily separate the WO_3/Fe_3O_4 catalysts is of great importance for many applications, their magnetic properties have been studied. The gravity deposition efficiency for all tested catalysts ranges from 5.20% ($0.4WO_3/Fe_3O_4$) to 21.53% ($6.1WO_3/Fe_3O_4$) after a time interval of 120 s (Fig. 15). Under the influence of an external magnetic field of 160 mT, a significant increase in the separation efficiency was observed. Increasing the content of WO_3 in the synthesized catalysts leads to an increase in the efficiency of magnetic separation. Even the smallest amount of tungsten added led to an increase in the efficiency of magnetic separation, which was almost 50% higher for the sample $0.4WO_3/Fe_3O_4$ compared to the unmodified Fe_3O_4. Further enhancement of WO_3 content to 1.4% leads to a slight increase in the magnetic separation efficiency to 58%, while further increases in the WO_3 content did not lead to significant changes in separation efficiency; 52.4% for $6.1WO_3/Fe_3O_4$ and 55.2% for $9.1WO_3/Fe_3O_4$.

On the other hand, the magnetic field has a somewhat different effect on the separation efficiency given a short separation time (up to 10 s). The most efficient magnetic field separation was achieved for the sample $6.1WO_3/Fe_3O_4$. In fact, the catalyst separation efficiency corresponds closely to the values for their saturation magnetisation presented in section 3.1.4. This order of separation efficiency, despite the increase for all catalysts, remains unchanged for up to 20 s of separation. It is clear that the influence of the external magnetic field during the initial separation phase is related to the magnetite phase content in each catalyst.

Comparing the efficiency of separation with and without the applied magnetic field, the positive effect of the external magnetic field is recognisable even over more prolonged separation times, but with a somewhat altered order of efficiency in the case of the short separation time. This suggests a slightly modified mechanism for the influence of the magnetic field on the catalyst separation from suspension over shorter and longer separation times.

It is known from the literature that a spin imbalance between the antiparallel octahedral and tetrahedral iron sublattices leads to the ferromagnetic properties of magnetite, as magnetic moments of ions in the octahedral sites (Fe^{2+} and Fe^{3+}) are aligned anti-ferromagnetically with ions in the tetrahedral sites (Fe^{3+}), resulting in the moments of the ferric ions efficiently cancelling each other out and leaving the net magnetic moment to be due to the Fe^{2+} octahedral ions. Consequently, the magnetic properties of magnetite are highly sensitive to changes in stoichiometry [70]. From this it can be concluded that the

26

presence of WO_3 in an appropriate amount affects the ratio of hematite to magnetite (Table 1), which probably changes the above-described stoichiometry. Thus, the efficiency of applying magnetic catalysts and implementing magnetic separation in AOPs is obvious.
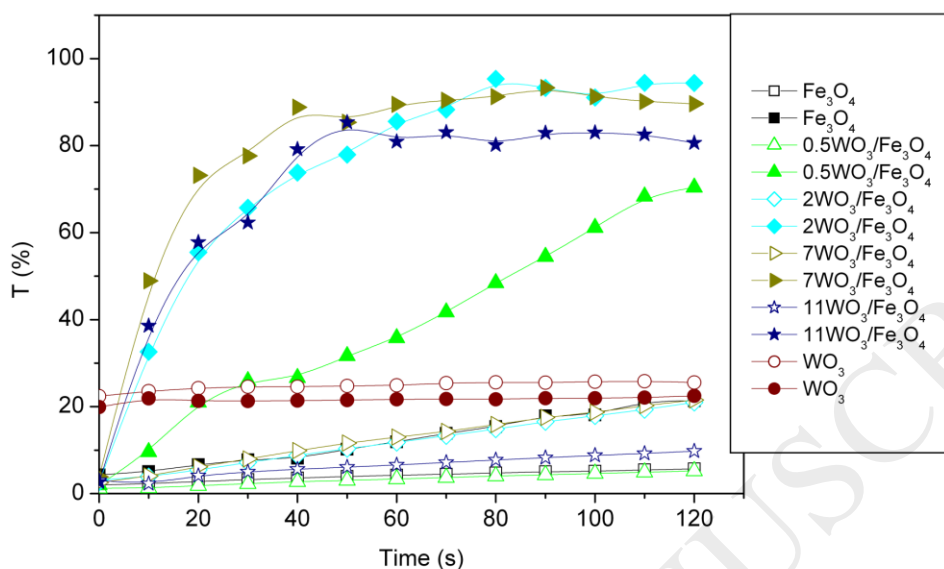

Fig. 15. Effect of WO_3 content on the efficiency of the magnetic separation of unsupported WO_3, unmodified Fe_3O_4 and catalysts (MF - filled symbols; GF - empty symbols). Operating conditions: photocatalysts = 1.67 g L^{-1}.

4. Conclusions

WO_3/Fe_3O_4 photocatalysts with different contents of WO_3 (0.37, 1.41, 6.13, and 9.11%, w/w) were successfully prepared by simple chemical co-precipitation method. The content of the magnetite phase in WO_3/Fe_3O_4 powders increased with increasing WO_3 content, and reached almost 80% for the $6.1WO_3/Fe_3O_4$, whereas the sample unmodified with WO_3 contains less than 10% magnetite after the synthesis procedure applied. The increasing content of WO_3 in the catalysts caused increases in all the textural parameters while their mesoporous structure was preserved. Effective charge carrier separation for the synthesized catalysts can be achieved using SS radiation. The photocatalytic efficiency of the powders was tested for the degradation of TCL under the influence of UV and SS radiation. The optimal mass ratio of WO_3 towards Fe_3O_4 in the presence of SS radiation was 6.1% and the optimal calcination temperature was 370 °C. The optimum catalyst loading was 0.42 g L^{-1} for $6.1WO_3/Fe_3O_4$ powder under UV radiation at pH 2.8. Under SS radiation using a heterogeneous photo-Fenton system with $6.1WO_3/Fe_3O_4/H_2O_2$ the degradation efficiency was 2.2 times greater compared to Fe_3O_4/H_2O_2. From the results obtained, it can be concluded that in addition to the significant influence of heterogeneous photo-Fenton

process, the effect of semiconductors coupling also affects the degradation efficiency to a large extent. Finally, the influence of the WO_3 content on the magnetic properties of WO_3/Fe_3O_4 powders was also examined, with modified spectrophotometric examinations revealing different mechanisms for short and long separation times.

Notes

The authors declare no competing financial interest.

Appendix A. Supplementary material

Supplementary material related to this article can be found, in the online version, at doi:

References

[1] W.X. Ping, S.D. Chao, Y.T. Dong, Sci. China 59 (2016) 1899.

[2] E. Brillas, C.A. Martínez-Huitle, Appl. Catal. B: Environ. 166–167 (2015) 603.

[3] R. Naidu, V.A.A. Espana, Y. Liu, J. Jit, Chemosphere 154 (2016) 350.

[4] World Health Organization, Drinking-water, Fact sheet.
   http://www.who.int/mediacentre/factsheets/fs391/en/, 2017 (accessed 22 January 2018).

[5] D. Shahidi, R. Roy, A. Azzouz, Appl. Catal. B Environ. 174–175 (2015) 277.

[6] J. Xiao, Y. Xie, H. Cao, Chemosphere 121 (2015) 1.

[7] M.N. Chong, B. Jin, C.W.K. Chow, C. Saint, Water Res. 44 (2010) 2997.

[8] Z. Zhang, J. Kong, J. Hazard. Mater. 193 (2011) 325.

[9] S. Zhang, H. Niu, Z. Hu, Y. Cai, Y. Shi, J. Chromatogr. A 1217 (2010) 4757.

[10] J. Tang, Z. Zou, J. Ye, Catal. Lett. 92 (2004) 53.

[11] S.G. Kumar, K.S.R. Koteswara Rao, RSC Adv. 5 (2015) 3306.

[12] M. Rahimi-Nasrabadi, M. Behpour, A. Sobhani-Nasab, M. Rangraz Jeddy, J. Mater. Sci: Mater. Electron. 27 (2016) 11691.

[13] F. Ahmadi, M. Rahimi-Nasrabadi, A. Fosooni, M. Daneshmand, J. Mater. Sci: Mater. Electron. 27 (2016) 9514.

[14] K.M. Lee, C.W. Lai, K.S. Ngai, J.C. Juan, Water Res. 88 (2016) 428.

[15] M. Rahimi-Nasrabadi, F. Ahmadi, A. Fosooni, J. Mater. Sci: Mater. Electron. 28 (2017) 537.

[16] A. Zapata, I. Oller, E. Bizani, J.A. Sánchez-Pérez, M.I. Maldonado, S. Malato, Catal. Today 144 (2009) 94.

[17] J.J. Pignatello, Environ. Sci. Technol. 26 (1992) 944.

[18] S. Malato, J. Blanco, A. Vidal, C. Richter, Appl. Catal. B Environ. 37 (2002) 1.

[19] R.H. Coupe, J.D. Blomquist, J. Am. Water Works Assoc. 96 (2004) 56.

[20] P. Jeschke, R. Nauen, M. Schindler, A. Elbert, J. Agric. Food Chem. 59 (2011) 2897.

[21] V. Guzsvány, J. Csanádi, F. Gaál, ActaChim. Slov. 53 (2006) 52.

[22] U. Černigoj, U. Lavrenčič Štangar, P Trebše, Appl. Catal. B Environ. 75 (2007) 229.

[23] M.L. Dell'Arciprete, L. Santos-Juanes, A. ArquesSanz, R. Vicente, A.M. Amat, J.P. Furlong, D.O. Mártire, M.C. Gonzales, Photochem. Photobiol. Sci. 8 (2009) 1016.

[24] U. Černigoj, U. Lavrenčič Štangar, J. Jirkovský, J. Hazard. Mater. 177 (2010) 399.

[25] B.F. Abramović, N.D. Banić, D.V. Šojić, Chemosphere 81 (2010) 114.

[26] N. Banić, B. Abramović, J. Krstić, D. Šojić, D. Lončarević, Z. Cherkezova-Zheleva, V. Guzsvány, Appl. Catal. B Environ. 107 (2011) 363.

[27] B.F. Abramović, N.D. Banić, J.B. Krstić, Ind. Eng. Chem. Res. 52 (2013) 5040.

[28] N.D. Banić, B.F. Abramović, D.V. Šojić, J.B. Krstić, N.L. Finčur, I.P. Bočković, Chem. Eng. J. 286 (2016) 184.

[29] N.D. Banić, D.V. Šojić, J.B. Krstić, B.F. Abramović, Water Air Soil Pollut. 225 (2014) 1954, 1.

[30] R.M. Cornell, U. Schwertmann, The Iron Oxides: Structure, Properties, Reactions, Occurrences and Uses, Wiley VCH, Weinheim (2003).

[31] M. Gotić, M. Ivanda, S. Popović, S. Musić, Mater. Sci. Eng. 77 (2000) 193.

[32] H. Zheng, J.Z. Ou, M.S. Strano, R.B. Kaner, A. Mitchell, K. Kalantar-zadeh, Adv. Funct. Mater. 21 (2011) 2175.

[33] R. Huirache-Acuña, F. Paraguay-Delgado, M.A. Albiter, J. Lara-Romero, R. Martínez-Sánchez, Mater. Charact. 60 (2009) 932.

[34] D. Sánchez-Martínez, A. Martínez-de la Cruz, E. López-Cuéllar, Mater. Res. Bull. 48 (2013) 691.

[35] R.W. Cheary, A.A. Coelho, J. Appl. Cryst. 25 (1992) 109.

[36] M. Thommes, K. Kaneko, A.V. Neimark, J.P. Olivier, F. Rodriguez-Reinoso, J. Rouquerol, K.S. Sing, Pure Appl. Chem. 87 (2015) 1051.

[37] M.M. Dubinin, Progress in Surface and Membrane Science, vol. 9, AcademicPress, NY, 1975.

[38] E.P. Barrett, L.G. Joyner, P.P. Halenda, J. Am. Chem. Soc. 73 (1951) 373.

[39] A. Lecloux, J.P. Pirard, J. Colloid Interface Sci. 70 (1979) 265.

[40] N. Banić, M. Vraneš, B. Abramović, J. Csanádi, S. Gadžurić, Dalton Trans. 43 (2014) 15515.

[41] W. Sun, M.T. Yeung, A.T. Lech, C.W. Lin, C. Lee, T. Li, X. Duan, J. Zhou, R.B. Kaner, Nano Lett. 15 (2015) 4834.

[42] A.C. Marques, L. Santos, M.N. Costa, J.M. Dantas, P. Duarte, A. Gonçalves, R. Martins, C.A. Salgueiro, E. Fortunato, Sci. Rep.-UK 5 (2015) 9910, 1.

[43] X. Cao, R. Prozorov, Y. Koltypin, G. Kataby, I. Felner, A. Gedanke, J. Mater. Res. 12 (1997) 402.

[44] A.-F. Lehlooh, S. Mahmood, I. Abu-Aljarayesh, J. Magn. Magn. Mater. 136 (1994) 143.

[45] E.R. Monazam, R.W. Breault, R. Siriwardane, Ind. Eng. Chem. Res. 53 (2014) 13320.

[46] B.D. Cullity, Introduction to Magnetism and Magnetic Materials, Addison-Wesley, MA, 1972.

[47] P. Guardia, A. Labarta, X. Batlle, J. Phys. Chem. C 115 (2010) 390.

[48] D. Thapa, V.R. Palkar, M.B. Kurup, S.K. Malik, Mater. Lett. 58 (2004) 2692.

[49] B. Andrzejewski, W. Bednarski, M. Kaźmierczak, A. Łapiński, K. Pogorzelec-Glaser, B. Hilczer, S. Jurga, G. Nowaczyk, K. Załęski, M. Matczak, B. Łęska, Compos. Part B-Eng. 64 (2014) 147.

[50] D. Caruntu, G. Caruntu, C.J. O'Connor, J. Phys. D Appl. Phys. 40 (2007) 5801.

[51] L. Zhuang, W. Zhang, Y. Zhao, H. Shen, H. Lin, J. Liang, Sci. Rep.-UK 5 (2015) 9320, 1.

[52] A.K. Singh, O.N. Srivastava, K. Singh, Nanoscale Res. Lett. 12 (2017) 298, 1.

[53] S. Malato, P. Fernández-Ibáñez, M.I. Maldonado, J. Blanco, W. Gernjak, Catal. Today 147 (2009) 1.

[54] M. Qamar, M. Muneer, Desalination 249 (2009) 535.

[55] A.N. Ejhieh, M. Khorsandi, J. Hazard. Mater. 176 (2010) 629.

[56] C.-H. Liang, M.-F. Hou, S.-G. Zhou, F.-B. Li, C.-S. Liu, T.-X. Liu, Y.-X. Gao, X.-G. Wang, J.-L. Lü, J. Hazard. Mater. 138 (2006) 471.

[57] S.S. Lin., M.D. Gurol, Environ. Sci. Technol. 32 (1998) 1417.

[58] N. Banić, B. Abramović, F. Šibul, D. Orčić, M. Watson, M. Vraneš, S. Gadžurić, RSC Adv. 6 (2016) 52826.

[59] N. Serpone, P. Maruthamuthu, P. Pichat, E. Pelizzetti, H. Hidaka, J. Photochem. Photobiol. A: Chem. 85 (1995) 247.

[60] Y. Bessekhouad, D. Robert, J.V. Weber, J. Photochem. Photobiol. A: Chem. 163 (2004) 569.

[61] M.I. Stefan, A.R. Hoy, J.R. Bolton, Environ. Sci. Technol. 30 (1996) 2382.

[62] B. Tryba, A.W. Morawski, M. Inagaki, M. Toyoda, Appl. Catal. B: Environ. 63 (2006) 215.

[63] H. Huang, X. Han, X. Li, S. Wang, P.K. Chu, Y. Zhang, ACS Appl. Mater. Interfaces 7 (2015) 482.

[64] H. Huang, K. Xiao, Y. He, T. Zhang, F. Dong, X. Du, Y. Zhang, Appl. Catal. B-Environ. 199 (2016) 75.

[65] H. Huang, K. Xiao, T. Zhang, F. Dong, Y. Zhang, Appl. Catal. B-Environ. 203 (2017) 879.

[66] W. Wu, C. Jiang, V.A.L. Roy, Nanoscale 7 (2015) 38.

[67] H. Huang, X. Li, J. Wang, F. Dong, P.K. Chu, T. Zhang, Y. Zhang, ACS Catal. 5 (2015) 4094.

[68] H. Huang, S. Tu, C. Zeng, T. Zhang, A.H. Reshak, Y. Zhang, Angew. Chem. Int. Ed. 56 (2017) 11860.

[69] T.L.P. Dantas, J.J. Humberto, R.F.P.M. Moreira, Acta Sci-Technol. 25 (2003) 91.

[70] J.M. Byrne, G. Van der Laan, A.I. Figueroa, O. Qafoku, C. Wang, C.I. Pearce, M. Jackson, J. Feinberg, K.M. Rosso, A. Kappler, Sci. Rep. 6 (2016) 30969, 1.